SCIENCE CHINA
Technological Sciences

Special Issue on Rock Fractures and Discontinuities: Modeling and Analysis
• Article •

September 2015 Vol.58 No.9: 1520–1532
doi: 10.1007/s11431-015-5900-6

Numerical manifold method based on isogeometric analysis

ZHANG YouLiang*, LIU DengXue & TAN Fei

State Key Laboratory of Geomechanics and Geotechnical Engineering, Institute of Rock and Soil Mechanics, Chinese Academy of Sciences, Wuhan 430071, China

Received April 15, 2015; accepted July 8, 2015; published online July 29, 2015

In this study, numerical manifold method (NMM) coupled with non-uniform rational B-splines (NURBS) and T-splines in the context of isogeometric analysis is proposed to allow for the treatments of complex geometries and local refinement. Computational formula for a 9-node NMM based on quadratic B-splines is derived. In order to exactly represent some common free-form shapes such as circles, arcs, and ellipsoids, quadratic non-uniform rational B-splines (NURBS) are introduced into NMM. The coordinate transformation based on the basis function of NURBS is established to enable exact integration for the manifold elements containing those shapes. For the case of crack propagation problems where singular fields around crack tips exist, local refinement technique by the application of T-spline discretizations is incorporated into NMM, which facilitates a truly local refinement without extending the entire row of control points. A local refinement strategy for the 4-node mathematical cover mesh based on T-splines and Lagrange interpolation polynomial is proposed. Results from numerical examples show that the 9-node NMM based on NURBS has higher accuracies. The coordinate transformation based on the NURBS basis function improves the accuracy of NMM by exact integration. The local mesh refinement using T-splines reduces the number of degrees of freedom while maintaining calculation accuracy at the same time.

numerical manifold method (NMM), isogeometric analysis, local refinement, mathematical cover

Citation: Zhang Y L, Liu D X, Tan F. Numerical manifold method based on isogeometric analysis. Sci China Tech Sci, 2015, 58: 1520–1532, doi: 10.1007/s11431-015-5900-6

1 Introduction

The presence of discontinuities such as joints, weak planes, weakness zones, and faults in a rock mass makes it different from other engineering materials. The mechanical behaviour of a rock mass is mainly controlled by discontinuities within the rock mass. Therefore, the capability to model discontinuities for a numerical method is crucial to produce satisfactory results. Numerical manifold method (NMM) proposed by Shi provides a unified mathematical framework for modelling the transition of rock masses from continuum state to discontinuum state [1, 2]. It has been widely used in geotechnical engineering for the small deformation analysis and large discontinuous displacement analysis [3–6].

The level of approximation of NMM can be improved in three ways [7]: Adopting higher order functions as its cover function, increasing the order of its weight function (known as p-refinement), and splitting the elements into smaller ones (known as h-refinement). The original NMM has only first-order accuracy, leading to dissatisfaction in simulating problems that need high accuracy in displacement representation [8]. Chen et al. [9] derived a high-order NMM formulation by using higher degree polynomials as the local approximations. However, this approach leads to the rank deficiency of the stiffness matrix and thus causes failure in solving the system of equations. With regard to the h-refinement, a cover refinement strategy is necessary when

*Corresponding author (email: ylzhang@whrsm.ac.cn)

simulating crack propagation in NMM. One traditional solution is to refine the entire mesh which can lead to a significant decrease in the computational efficiency. Tesay et al. [10], Chiou et al. [11], and Yang et al. [12] investigated triangular mesh-based local refinement algorithms and achieved better results. However, when meshes are refined using regular rectangle-based NMM, hanging nodes exist which are difficult to handle.

On the other hand, there is still a gap for NMM to be used in industrial applications which utilize Computer Aided Design (CAD) as a basic tool. The CAD representations of objects are composed of a collection of complex curves and surfaces which can not be directly and exactly imported into the NMM program. Errors occur when the solution is sensitive to geometry description such as shell buckling. Isogeometric analysis, proposed by Hughes et al. [13–16] in 2005, is a numerical analysis method, which combines CAD with computer aided engineering (CAE). Its basic idea is to apply the same basis function for geometric modelling and unknown variables. The most common basis function is the non-uniform rational B-splines (NURBS), which show many advantages [17]: Modelling for any surface and possessing superior mathematical characteristics, including non-negativity, partitioning of unit, linear independence of basis function, local support, etc. However, NURBS do not support local refinement which limits their use. The refinement using NURBS requires the insertion of an entire row (or column) of control points. This means that a large percentage of control points is redundant because they need only to satisfy the topological constraint. To overcome this limitation, Sederberg invented T-splines [18,19]. T-splines [18] are an extension of NURBS. Apart from the advantages of NURBS, T-splines present typical advantages; they are more suitable for local mesh refinement and can remove the interval or overlap from the junction between surfaces. Bazilevs et al. [20] explored isogeometric analysis based on the basis function of T-splines and applied this method to simple calculations in fluid and structural mechanics.

In this paper, non-uniform rational B-splines (NURBS) under the context of isogeometric analysis are introduced into NMM. The coordinate transformation based on the basis function of NURBS is established to enable exact integration for the manifold elements containing those shapes. For the problems of crack propagation where singular fields around crack tips exist, local refinement technique by the application of the T-spline discretizations is incorporated into NMM, which facilitates a truly local refinement. This paper is organized as follows. In Section 2, basic theories of NMM are briefly reviewed. Section 3 illustrates B-Splines and NURBS. In Section 4, NURBS are introduced into NMM. The coordinate transformation based on NURBS is established in Section 5. Section 6 discusses local refinement based on T-Splines. In Section 7 three numerical experiments are carried out. Finally, Section 8 provides some concluding remarks.

2 Basic theories of NMM

2.1 The finite cover system in NMM

NMM is established on the basis of three important concepts: mathematical cover (MC), physical cover (PC), and manifold element (ME). The MC system is the union of patches which overlap partially or completely and it must be large enough to cover the whole problem domain. Each patch is defined as a MC, denoted by M_i (i = 1–n_{M}, where n_{M} is the number of MCs for the problem). The PC system is formed by intersecting MCs with different types of boundaries such as material boundaries, cracks, external boundary and internal discontinuities. PCs are denoted by p^i_j (j = 1–n_{p}, where n_{p} is the number of MCs for the problem). The common area of several PCs forms a ME.

To clearly explain the three concepts, an example is given (Figure 1). For the irregular polygon plate containing one crack in Figure 1, the MC system adopts a regular rectangular mesh; four rectangles with common node i form a MC, which is denoted by M_i. M_1 and the crack intersect to constitute two physical covers p_1^1 and p_1^2. M_2, M_3, M_4, and M_5, without intersection with physical meshes, form PCs p_2, p_3, p_4 and p_5 separately. Thus, PCs and MCs are identical. As shown by the shaded area in Figure 1, manifold element $E(p_2, p_3, p_4, p_5)$ is the common part of p_2, p_3, p_4, and p_5 while element $E(p_6, p_7, p_8, p_9)$ denotes the common part of p_6, p_7, p_8, and p_9. The shape of ME is arbitrary while the corresponding PC is unique.

2.2 The mathematical cover based on rectangle mesh

On each M_i, a weight function $\varphi_i(x)$ is defined to specify the interpolation which satisfies the following properties:

$$0 \leqslant \phi_i(x,y) \leqslant 1, \quad (x,y) \in M_i, \tag{1}$$

$$\phi_i(x,y) = 0, \quad (x,y) \notin M_i, \tag{2}$$

$$\sum_{\{(x,y)\in M_k\}} \phi_k(x,y) = 1. \tag{3}$$

Eqs. (1) and (2) indicate that the weight function has non-

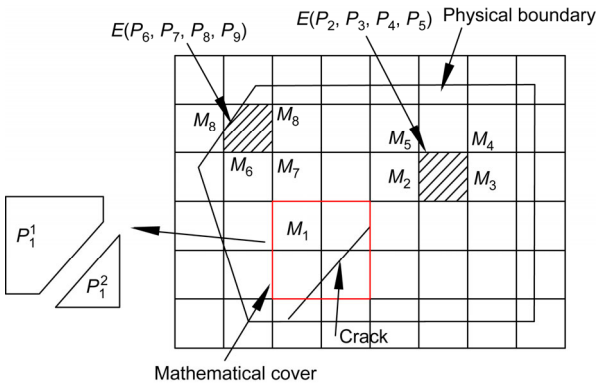

Figure 1 Covers and elements in NMM.

zero values inside M_i, and zero values outside. Eq. (3) is the partition of unity property which constructs the global approximation by pasting the local approximation spaces.

Theoretically any shape of MCs can be used in NMM because MCs are independent of the physical domain. The only requirement is that their union must be large enough to cover the entire problem domain. However, for the sake of simplicity in constructing the weight functions and implementing the computer code, a triangular or quadrilateral mesh is usually adopted to define MC for 2-dimensional problems. In this study, a regular and fixed rectangular mesh is used considering its convenient meshing procedures. In this case, a MC is composed of four rectangular elements, as shown in Figure 1. The common node of the four rectangular elements is regarded as a star. For the case of rectangular MC whose edges are parallel to the axes in global coordinate system, as shown in Figure 2, the weight function can be defined as [21]

$$\begin{cases} \phi_1(x,y)=\dfrac{1}{4}\left(1+\dfrac{2x'}{a}\right)\left(1+\dfrac{2y'}{b}\right), \\ \phi_2(x,y)=\dfrac{1}{4}\left(1-\dfrac{2x'}{a}\right)\left(1+\dfrac{2y'}{b}\right), \\ \phi_2(x,y)=\dfrac{1}{4}\left(1-\dfrac{2x'}{a}\right)\left(1-\dfrac{2y'}{b}\right), \\ \phi_2(x,y)=\dfrac{1}{4}\left(1-\dfrac{2x'}{a}\right)\left(1-\dfrac{2y'}{b}\right), \end{cases} \tag{4}$$

with relative coordinates to the centre of the rectangle being

$$\begin{cases} x'=x-\dfrac{x_1+x_2}{2}, \\ y'=y-\dfrac{y_1+y_2}{2}. \end{cases} \tag{5}$$

2.3 Displacement function and modelling of discontinuities in NMM

On each PC, a local displacement function is defined. The displacement function can be constant, linear, high-order polynomials or a local series. In the original NMM, a constant cover function is defined as

$$\begin{Bmatrix} u_i^j(x,y) \\ v_i^j(x,y) \end{Bmatrix}=\begin{bmatrix} 1 & 0 \\ 0 & 1 \end{bmatrix}\begin{Bmatrix} d_{i1}^j \\ d_{i2}^j \end{Bmatrix}=[\boldsymbol{C}]\{d_i^j\}, \tag{6}$$

where d_i^j is the vector of unknowns.

After defining the weight functions $\varphi_i(x)$ and the cover functions, the function for the overall displacement of the whole material is expressed as

$$\begin{Bmatrix} u(x,y) \\ v(x,y) \end{Bmatrix}=\sum_{\substack{i \\ if\ e\subset p_i^j}}^{n}\phi_i(x,y)\begin{Bmatrix} u_i^j(x,y) \\ v_i^j(x,y) \end{Bmatrix}, \tag{7}$$

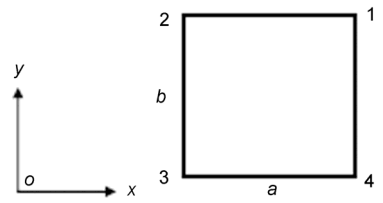

Figure 2 A rectangular element from Figure 1 with its four MCs represented by their centre point.

where n is the number of PCs sharing the ME e, $\varphi_i(x)$ is the weight function corresponding to the PC p_j^i, which is the same as that defined on M_i.

When modelling strong discontinuity problems where singularities exist at crack tips, polynomials can not accurately represent the local characteristics and thus lead to a poor approximation of the solution. Hence, a prior known knowledge about the solution can be adopted to customize the cover functions. As shown in Figure 3, M_1, M_2, M_3, and M_4 containing the crack tip forms only one whole PC respectively. These PCs are called singular PC in ref. [22]. The common area of these PCs forms the element $E(p_1, p_2, p_3, p_4)$. For these singular PCs the cover functions are enriched in a similar manner mentioned in ref. [23]. The displacement approximation in eq. (7) can be enriched as

$$\begin{Bmatrix} u(x,y) \\ v(x,y) \end{Bmatrix}=\sum_{\substack{i \\ if\ e\subset p_i^j}}^{n}\phi_i(x,y)\begin{Bmatrix} u_i^j(x,y) \\ v_i^j(x,y) \end{Bmatrix}+\sum_{j=1}^{n_s}\phi_j(x,y)U_j, \tag{8}$$

where the additional cover function U_j for singular PCs is

$$U_j=\boldsymbol{\Phi}c_j, \tag{9}$$

where c_j is the array of additional unknowns, and n_s is the number of singular PCs associated with the ME e. $\boldsymbol{\Phi}$ is the matrix of singular basis shown as

$$\boldsymbol{\Phi}=\begin{bmatrix} \Phi_1 & 0 & \Phi_2 & 0 & \Phi_3 & 0 & \Phi_4 & 0 \\ 0 & \Phi_1 & 0 & \Phi_2 & 0 & \Phi_3 & 0 & \Phi_4 \end{bmatrix}, \tag{10}$$

with

$$\begin{bmatrix} \Phi_1 & \Phi_2 & \Phi_3 & \Phi_4 \end{bmatrix}= \\ \begin{bmatrix} \sqrt{r}\sin\dfrac{\theta}{2} & \sqrt{r}\cos\dfrac{\theta}{2} & \sqrt{r}\sin\theta\sin\dfrac{\theta}{2} & \sqrt{r}\sin\theta\cos\dfrac{\theta}{2} \end{bmatrix}, \tag{11}$$

where (r, θ) are the polar coordinates in the local system with the origin located at the crack tip. It is noted that the four basis functions can construct arbitrary displacement field near the crack tip. Based on the enriched technique, crack tips can locate at arbitrary positions in a manifold element, and the stress intensity factors (SIFs) can be accurately evaluated with a regular and relatively coarse MC system [24].

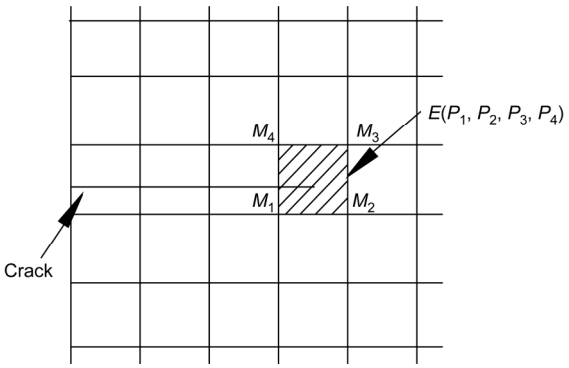

Figure 3 Singular PCs at crack tip in 4-node NMM.

3 Introduction of B-splines and NURBS

Owing to the basis function of NURBS being linear combination of the basis functions of B-splines, the basis function of B-splines is first described.

3.1 B-splines

The basis function of B-splines is defined on a knot vector whose parameter space is known. Let $\boldsymbol{U} = \{u_1, u_2,\cdots, u_{n+p+1}\}$ be a non-decreasing real sequence, namely, $u_i \leqslant u_{i+1}$, $i = 1, 2,\cdots,n + p + 1$, where u_i is defined as the knot; p refers to its order; n is the number of basis functions for constructing B-splines curve; and $\boldsymbol{U}$ is a knot vector. When knot vector $\boldsymbol{U}$ is given, the basis function of B-splines is defined by the Cox-de Boor recurrence formula [25,26].

$$N_{i,0}(u) = \begin{cases} 1, & \text{if } u_i \leqslant u < u_{i+1}, \\ 0, & \text{otherwise}, \end{cases} \tag{12}$$

$$N_{i,p}(u) = \frac{u-u_i}{u_{i+p}-u_i} N_{i,p-1}(u) + \frac{u_{i+p+1}-u}{u_{i+p+1}-u_{i+1}} N_{i+1,p-1}(u), \quad (p \geqslant 1). \tag{13}$$

The basis function of the B-splines is characterised by:

(1) B-splines basis functions constitute a partition of unity, namely,

$$\sum_{i=1}^{n} N_{i,p}(u) = 1, \quad u \in [u_1, u_{n+p+1}].$$

(2) Each basis function is non-negative,

$$N_{i,p}(u) \geqslant 0, \quad u \in [u_i, u_{i+p+1}].$$

(3) Basis functions are linear independent, i.e.

$$\sum_{i=1}^{n} \alpha_i N_{i,p}(u) = 0 \Leftrightarrow \alpha_k = 0,\ k = 1,2,\cdots,n.$$

(4) Compact support.

$$\{u \mid N_{i,p}(u) > 0\} \subset [u_i, u_{i+p+1}].$$

(5) Differentiability. If the multiplicity of one knot value is k (i.e., $u_i=u_{i+1}=\cdots=u_{i+k+1}$), the basis function at this point is C^{p-k} continuous.

By defining d_s as a space dimension, the B-splines curve in space $\boldsymbol{R}^{\mathrm{ds}}$ is linearly defined by the basis function of B-splines

$$C(u) = \sum_{i=0}^{n} N_{i,p}(u)\boldsymbol{B}_i, \tag{14}$$

where $\boldsymbol{B}_i$ refers to the control point and i = 1, 2,···, n; $N_{i,p}$ denotes the p order basis function of the B-splines which is defined on knot vector $\boldsymbol{U}=\{u_1, u_2,\cdots, u_{n+p+1}\}$ and i = 1, 2,···, n: the polygon constructed by $\boldsymbol{B}_i$ is the control polygon.

The B-splines surface is defined by the control point mesh in two directions, two knot vectors, and the tensor product of the single variable of the basis function of the B-splines. When one control point mesh $\{\boldsymbol{B}_{i,j}\}$ (i=1, 2,···, n and j=1, 2,···, m), two knot vectors $\boldsymbol{U}=\{u_1, u_2,\cdots, u_{n+p+1}\}$ and $\boldsymbol{V}=\{v_1, v_2,\cdots, v_{n+p+1}\}$ are known, the B-splines surface is expressed as

$$S(u,v) = \sum_{i=1}^{n}\sum_{j=1}^{m} N_{i,p}(u)N_{j,p}(v)\boldsymbol{B}_{i,j}, \tag{15}$$

where $N_{i,p}(u)$ and $N_{j,p}(v)$ are the basis functions of the B-splines surface.

3.2 NURBS

Although the B-splines can express curves and surfaces, they cannot accurately express many common geometries in engineering design, such as arcs, hyperbolae, and ellipses. To overcome this shortfall, rational B-splines are used. NURBS in n dimensional space are obtained by means of the projection of the B-splines in n+1 dimensional space. The establishment of rational B-splines is discussed below. By defining $\{\boldsymbol{B}_i{}^w\}$ as the set of the control points in $\boldsymbol{R}^{\mathrm{ds+1}}$ of the B-splines curve and its knot vector as $\boldsymbol{U}$, the control points in $\boldsymbol{R}^{\mathrm{ds}}$ of the NURBS curve are obtained according to eqs. (16) and (17):

$$\left(\boldsymbol{B}_i\right)_j = \left(\boldsymbol{B}_i^w\right)_j / w_i, \qquad i = 1,\cdots,d_s, \tag{16}$$

$$w_i = \left(\boldsymbol{B}_i^w\right)_{\mathrm{ds}+1}, \tag{17}$$

where $(\boldsymbol{B}_i)_j$ is the j^{th} component of vector $\boldsymbol{B}_i$; and w_i denotes the i^{th} weight. The basis functions of the rational B-splines and NURBS curve are expressed as follows:

$$R_{i,n}(u) = \frac{N_{i,n}(u)w_i}{\sum_{j=0}^{n} N_{j,n}(u)w_j}, \tag{18}$$

$$\mathrm{C}(u)=\sum_{i=0}^{n}R_{i,p}(u)\boldsymbol{B}_i. \tag{19}$$

Likewise, the basis function of the rational B-splines surface is

$$R_{i,j}(u,v)=\frac{N_{i,n}(u)N_{j,m}(v)w_{i,j}}{\sum_{\hat{i}=0}^{n}\sum_{\hat{j}=0}^{m}N_{\hat{i},n}(u)N_{\hat{j},m}(v)w_{\hat{i},\hat{j}}}. \tag{20}$$

The basis function of NURBS shows many characteristics of the basis function of B-splines, including normalisation, differentiability, compact support, etc. When the weights of the basis function are equal, NURBS degrade to B-splines.

4 Nine-node NMM based on quadratic NURBS

The higher order displacement function can be established by improving the order of the weight function. Owing to the weight function being defined on the MC, if the weight function is changed, the structural form of MC also needs to be changed to satisfy eqs. (1)–(3). The basis function of quadratic NURBS is taken as the weight function and the MC system adopts regular rectangular meshes, as illustrated in Figure 4. The adjacent nine rectangular meshes form a MC, as shown in Figure 5. For the sake of convenience, the mid-point of MC is deemed to represent the entire MC. ME marked in Figure 4 is the common part of the PCs formed by the nine MCs (as marked by black dots).

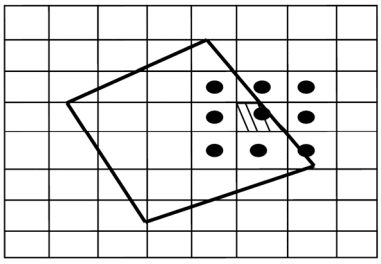

Figure 4 MC system in 9-node NMM.

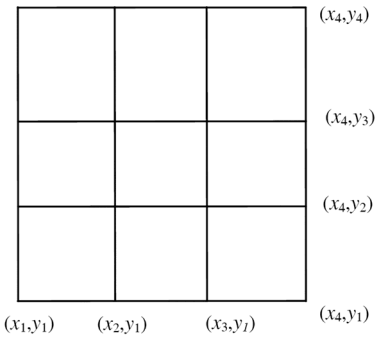

Figure 5 An MC in 9-node NMM.

For MCs shown in Figure 5, $\{x_1, x_2, x_3, x_4\}$ and $\{y_1, y_2, y_3, y_4\}$ are non-decreasing real sequences in the x- and y-directions respectively; the corresponding weight functions are derived according to eqs. (12), (13), and (20) where the values of m and n are 2, and the value of weight w is 1. The weight function is

$$\phi(x,y)=X(x)Y(y),\quad (x_1\leqslant x\leqslant x_4, y_1\leqslant y\leqslant y_4), \tag{21}$$

$$X(x)=\begin{cases}\dfrac{(x-x_1)(x-x_1)}{(x_3-x_1)(x_2-x_1)}, & x_1\leqslant x<x_2,\\ \dfrac{(x-x_1)(x_3-x)}{(x_3-x_1)(x_3-x_2)}+\dfrac{(x_4-x)(x-x_2)}{(x_4-x_2)(x_3-x_2)}, & x_2\leqslant x<x_3,\\ \dfrac{(x_4-x)(x_4-x)}{(x_4-x_3)(x_4-x_2)}, & x_3\leqslant x\leqslant x_4,\end{cases} \tag{22}$$

$$Y(y)=\begin{cases}\dfrac{(y-y_1)(y-y_1)}{(y_3-y_1)(y_2-y_1)}, & y_1\leqslant y<y_2,\\ \dfrac{(y-y_1)(y_3-y)}{(y_3-y_1)(y_3-y_2)}+\dfrac{(y_4-y)(y-y_2)}{(y_4-y_2)(y_3-y_2)}, & y_2\leqslant y<y_3,\\ \dfrac{(y_4-y)(y_4-y)}{(y_4-y_3)(y_4-y_2)}, & y_3\leqslant y\leqslant y_4.\end{cases} \tag{23}$$

The weight function has the following properties.

(1) Any point (x, y) in ME satisfies the partition of unit, shown as eq. (3).

(2) Each weight function, in its coverage area, is non-negative.

$$\phi_i(x,y)\geqslant 0,\quad (x,y)\in M_i. \tag{24}$$

(3) The weight function is C^1 continuous.

For NMM based on the basis function of quadratic NURBS, each ME is the common part of the corresponding nine PCs. The cover of the same mathematical mesh is realised by taking the common Lagrange interpolation function in FEM as the weight function in NMM. MC is shown in Figure 1 and ME formed is the common part of the corresponding four physical covers. The two aforementioned methods are named the 9-node NMM and 4-node NMM respectively. The weight distributions in the respective MC domain of the two methods are demonstrated in Figure 6.

Compared with the 4-node NMM when modeling strong discontinuity problems, difference exists as shown in Figure 7. Nine MCs containing crack tip, marked by black dots, forms one singular PC respectively. The cover function of these PCs is enriched in the same way described in Section 2.3. It is obvious that the domain affected by the enriched function in the 9-node NMM, under the same mathematical mesh, is bigger than that in the 4-node NMM.

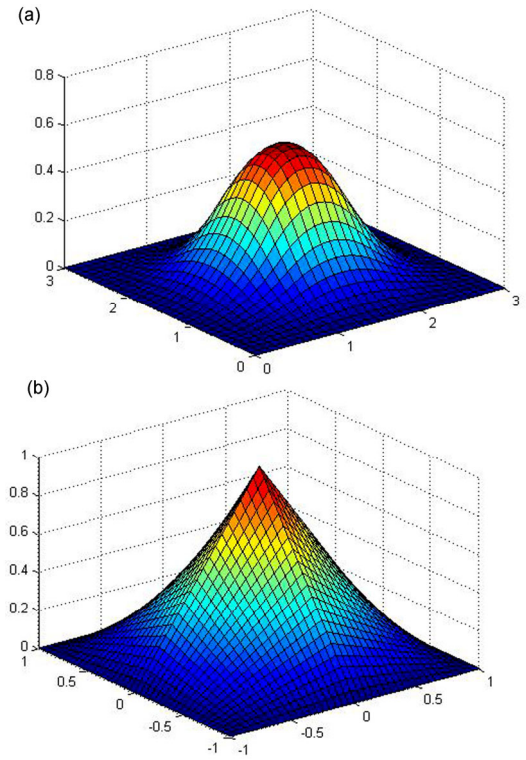

Figure 6 (a) Distribution of weights in an MC of 9-node NMM with $\{x_1,x_2,x_3,x_4\}=\{0,1,2,3\}$ $\{y_1,y_2,y_3,y_4\}=\{0,1,2,3\}$; (b) distribution of weights in an MC of 4-node NMM.

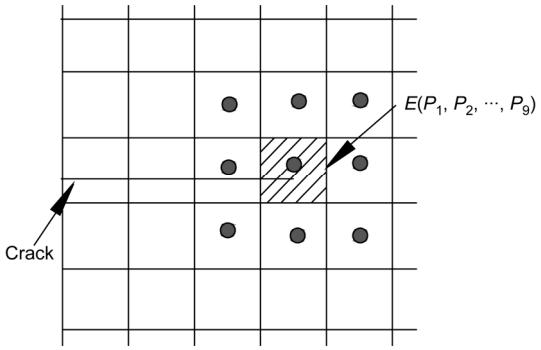

Figure 7 Singular PCs at crack tip in 9-node NMM.

5 Handling of the arc-contained boundary problem using NMM

According to traditional numerical analysis methods, integration points are arranged through coordinate transformation based on Lagrange, Legendre, or Hermite polynomial interpolation functions. However, these polynomial interpolation functions fail to accurately describe the curves of an arc, hyperbola, ellipse, etc. For boundary problems containing such curves, traditional numerical analysis methods need to simplify the actual geometry, thereby inducing error.

Based on isogeometric concepts, Section 5 suggests expressing a curved boundary with the NURBS curve. As mentioned in Section 2.2, NURBS can accurately describe arc, hyperbola, and ellipse by rationally arranging control points and adjusting their corresponding weights. Thus, the error caused by geometrical approximation of these curve boundaries is avoided.

5.1 Arc description using NURBS curve

Any minor arc in Figure 8 can be described by the NURBS curve (eq. (14)), where

$$N_{0,2}(u)=(1-u)^2 N_{1,2}(u)=2u(1-u)N_{2,2}(u)=u^2, \quad (25)$$

$$w_0=1,\ w_1=\cos\theta,\ w_2=1. \quad (26)$$

Control points B_0 and B_2 are two endpoints on the arc, and B_1 is the intersection point of the tangent lines to the two endpoints.

5.2 Handling of manifold elements with an arc edge

For ME with arc edge in Figure 9, the mid-point C is used to form triangles. For three triangles without arc edge, ordinary isoparametric transformation is used for numerical integration [27].

(1) For the three triangles without arc edge, coordinate transformation is performed to arrange numerical integration points, as shown in Figure 10.

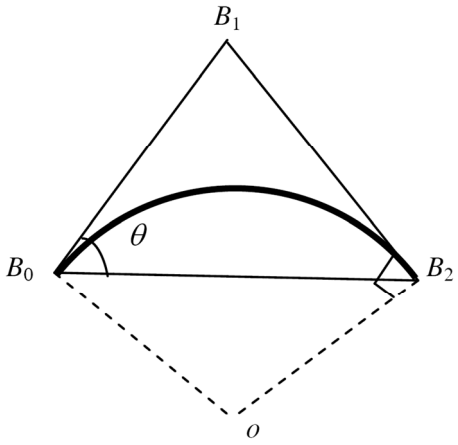

Figure 8 Arc described by NURBS.

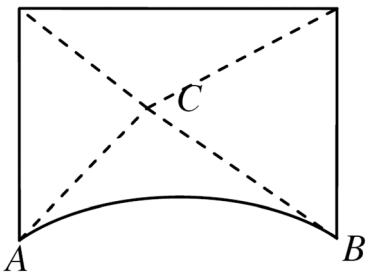

Figure 9 Element containing arc boundary.

The equation is

$$\begin{cases} x = \sum_{i=1}^{4} \varphi_i(\xi,\eta) x_i, \\ y = \sum_{i=1}^{4} \varphi_i(\xi,\eta) y_i. \end{cases} \tag{27}$$

(x_i, y_i) is the coordinate in the global coordinate system of triangle vertices, and the shape function $\phi_i(\xi, \eta)$ is

$$\varphi_i(\xi,\eta) = \frac{1}{4}(1+\xi_i\xi)(1+\eta_i\eta). \tag{28}$$

(ξ_i, η_i) are the coordinates of the four vertices of the quadrangle in ξ-η space.

(2) The triangle *ABC* containing an arc edge is expressed by the NURBS surface, and the expression for its basis function is given by eq. (20). In the *u*-direction, the arc curve is expressed by the second order NURBS curve mentioned in Section 5.1 while in the *v*-direction, the arc is expressed by the first order NURBS curve. Numerical integration over the triangle is realised through two different coordinate transformations, as illustrated in Figure 11.

The transformation from parameter space to physical area is expressed by

$$\begin{cases} x = \sum_{i=0}^{2}\sum_{j=0}^{1} R_{i,j}(u,v) x_{i,j}, \\ y = \sum_{i=0}^{2}\sum_{j=0}^{1} R_{i,j}(u,v) y_{i,j}. \end{cases} \tag{29}$$

The Jacobian matrix of the transformation is

$$\boldsymbol{J}_u = \begin{bmatrix} \sum_{i=0}^{2}\sum_{j=0}^{1} \frac{\partial R_{i,j}(u,v)}{\partial u} x_{i,j} & \sum_{i=0}^{2}\sum_{j=0}^{1} \frac{\partial R_{i,j}(u,v)}{\partial u} y_{i,j} \\ \sum_{i=0}^{2}\sum_{j=0}^{1} \frac{\partial R_{i,j}(u,v)}{\partial v} x_{i,j} & \sum_{i=0}^{2}\sum_{j=0}^{1} \frac{\partial R_{i,j}(u,v)}{\partial v} y_{i,j} \end{bmatrix}, \tag{30}$$

where the expressions for $R_{i,j}(u, v)$ and $N_{i,n}(u)$ are eqs. (20) and (25) respectively; $x_{i,j}$ and $y_{i,j}$ are the coordinates of the control point. The control point is shown in Figure 9(a). $N_{j,n}$ (v) is expressed as follows:

$$N_{0,1}(v) = 1 - v, \quad N_{1,1}(v) = v. \tag{31}$$

The transformation from parent element to parameter space is given by

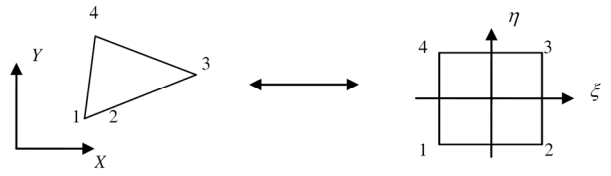

Figure 10 Coordinate transformation between triangular and quadrilateral elements.

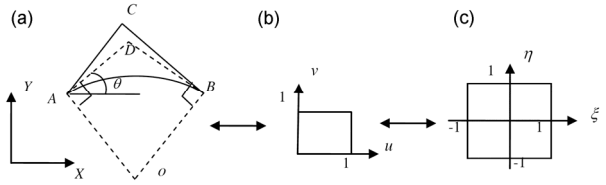

Figure 11 Transformation from physical domain to parent element. (a) Physical domain; (b) parametric space; (c) parent element.

$$\begin{cases} u = \dfrac{(\xi+1)}{2}, \\ v = \dfrac{(\eta+1)}{2}. \end{cases} \tag{32}$$

Jacobian matrix $\boldsymbol{J}_\xi$, is

$$\left|\boldsymbol{J}_\xi\right| = \frac{1}{4}. \tag{33}$$

The binary function f (x, y) is taken as an example for subsequent discussion of the integration process.

$$\begin{aligned} \int_\Omega f(x,y)\mathrm{d}\Omega &= \int_{\Omega_u} f(x(u,v),y(u,v))\left|\boldsymbol{J}_u\right|\mathrm{d}\Omega_u \\ &= \int_{\Omega_\xi} f(x(\xi,\eta),y(\xi,\eta))\left|\boldsymbol{J}_u\right|\left|\boldsymbol{J}_\xi\right|\mathrm{d}\Omega_\xi, \end{aligned} \tag{34}$$

where Ω is the physical area of triangle *ABC*, Ω_u denotes the parameter space, and Ω_ξ refers to the parent space.

6 Local mesh refinement using the 4-node NMM

With regard to classical mesh refinement in NMM, global refinement is required as shown in Figure 12(a). In this case, some refined elements are abundant. When local refinement shown in Figure 12(b) is adopted, T-junctions, corresponding "hanging node" in FEM, are produced. Misconduct of such nodes results in inaccurate calculations of displacement and stress. However, this problem can be solved by the proposed mathematical mesh refinement based on the T-splines concepts in this section.

6.1 Determination of MC after refinement

Four T-junctions are formed by local refinement of the central mesh, as presented in Figure 13(a). Each point in Figure 13(a) represents a MC, including four T-junctions. After refinement, a MC is determined as follows: by extension from the representative point of MC in all the four (up, down, right and left) directions, the first orthogonal mesh line encountered is then the MC boundary. By taking MC marked by the black dots in Figure 13(b) as an example, the red area represents the mathematical cover area. After de-

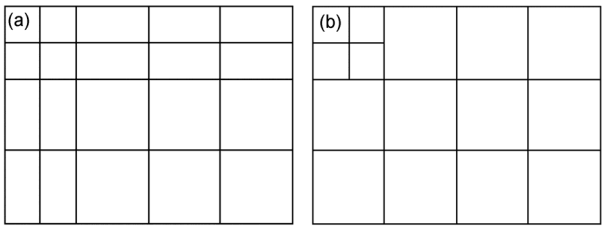

Figure 12 (a) Global refinement of mathematical mesh; (b) local refinement of mathematical mesh.

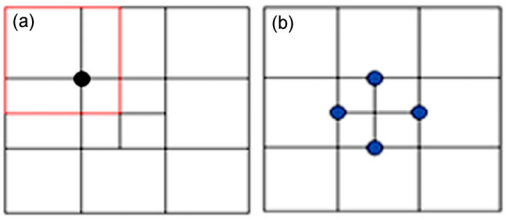

Figure 13 (a) Local refinement for mathematical mesh and four T-junctions exist marked by green dots; (b) definition of a mathematical cover for refined mesh.

termining MC, the PC and ME can be found accordingly.

6.2 Weight function for the refined MC

The weight distribution function on MC is defined by the basis function of the B-splines surface. For MC in Figure 14, $\{x_1, x_2, x_3\}$ and $\{y_1, y_2, y_3\}$ are non-decreasing real sequences in the x- and y-directions, respectively. According to eqs. (12) and (13), the weight distribution function is expressed as

$$\phi(x,y)=X(x)Y(y),\quad (x_1\leqslant x\leqslant x_3, y_1\leqslant y\leqslant y_3), \tag{35}$$

$$X(x)=\begin{cases}\dfrac{x-x_1}{x_2-x_1}, & x_1\leqslant x<x_2,\\ \dfrac{x_3-x}{x_3-x_2}, & x_2\leqslant x\leqslant x_3,\end{cases} \tag{36}$$

$$Y(y)=\begin{cases}\dfrac{y-y_1}{y_2-x_1}, & y_1\leqslant y<y_2,\\ \dfrac{y_3-y}{y_3-y_2}, & y_2\leqslant y\leqslant y_3.\end{cases} \tag{37}$$

The weight function shows interpolation property. It satisfies the partition of the unit, and it is also non-negative within MC.

7 Numerical examples

7.1 Infinite plate with a central circular hole

As shown in Figure 15(a), an infinite plate with a central

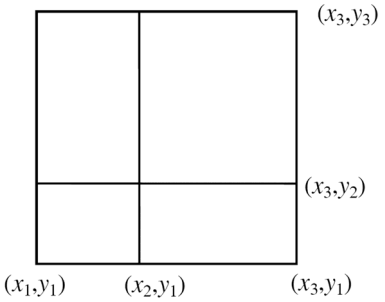

Figure 14 One mathematical cover.

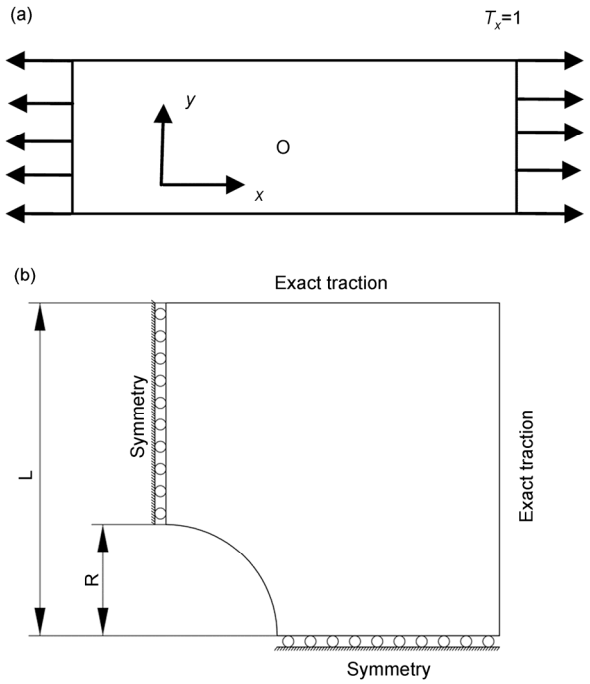

Figure 15 (a) Infinite plate with a circular hole under unidirectional tension; (b) part of infinite plate with displacement and stress boundary.

circular hole whose radius is 1, is subjected to a uniform tension in the x-direction. The distribution intensity of the tension is unity. The exact solution of the problem, in polar coordinates, is [28]

$$\sigma_r=\frac{1}{2}\left(1-\frac{1}{r^2}\right)+\frac{1}{2}\left(1+\frac{3}{r^4}-\frac{4}{r^2}\right)\cos(2\theta), \tag{38}$$

$$\sigma_\theta=\frac{1}{2}\left(1+\frac{1}{r^2}\right)-\frac{1}{2}\left(1+\frac{3}{r^4}\right)\cos(2\theta), \tag{39}$$

$$\tau_{r\theta}=-\frac{1}{2}\left(1-\frac{3}{r^4}+\frac{2}{r^2}\right)\sin(2\theta). \tag{40}$$

Considering symmetry, one fourth of the infinite plate is taken for calculation. Model parameters include R = 1 and L = 3. Plane strain condition is assumed, and the Young's modulus E is 1000, Poisson's ratio v is 0.3. The boundary

condition of the left displacement is $u = 0$, and the boundary condition of the bottom displacement is $v = 0$. According to the theoretical solution, the stresses on the upper and right boundaries are obtained and the stress boundary conditions are applied on the two boundaries, as shown in Figure 15(b).

After inputting the geometric parameters of the problem, the arc edge cannot be described accurately and thus, geometrical approximation is needed. The strategy for this problem replaces the arc by several line segments on the arc. And apparently this is an approximate method. Different numbers of points, shown in Figure 16, are arranged on the arc and the mathematical mesh which has 556 degrees of freedom (DOFs) for the 4-node NMM and 616 DOFs for the 9-node NMM, shown in Figure 20(a), is adopted.

The stress σ_x in the x-direction at the top point of the arc is ascertained and the result is shown in Figure 17: with more points arranged on the arc, the error in the two NMM methods gradually decreases; when the number of points increases to certain value, the error tends to be stable. It is noted that when the number of points in the arc is less than 16, the error calculated by the 9-node NMM is almost 2

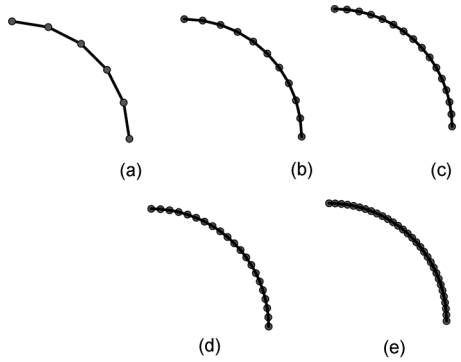

Figure 16 Arc edge in Figure 16 represented by connecting adjacent points on the arc. (a) 6 points; (b) 11 points; (c) 16points; (d) 21 points; (e) 31points.

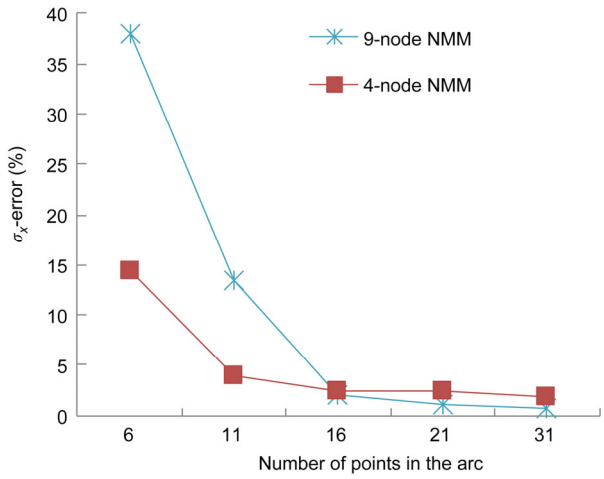

Figure 17 Relation between σ_x at top of the arc and the number of point in the arc.

times of that by the 4-node NMM. The reason is that: σ_x at top of the arc is related to the unknowns of the corresponding PCs. When using mathematical mesh with the same density, the affected area containing the approximate arc in the 9-node NMM is greater than that in the 4-node NMM. With increase in the number of points in the arc, the effect decreases.

31 points are arranged on the arc edge which is approximated and replaced by 30 line segments. Adopting the same regular rectangular mathematical meshes, stress (σ_x) is calculated using the 4-node and 9-node NMMs separately, as shown in Figure 18. These indicate that the stress distribution calculated using the latter method is smoother.

Two mesh refinement methods are adopted, as shown in Figure 19: (a) Entailed global refinement using the 4-node and 9-node NMMs respectively; (b) entailed local refinement using the 4-node NMM based on the treatment mentioned in Section 6. ME containing the arc edge was handled using the method presented in Section 5.2 so as to accurately describe the arc. The NMM method adopting this method is called the 4-node NMM_(improved) or 9-node NMM_(improved).

Figure 20 shows the calculation errors of several NMMs for different mathematical mesh densities. It reveals that with the denser mesh, the errors in these methods gradually decrease. The slopes of the six error curves are different: the slope of the 9-node NMM error curve is greater than that for the 4-node NMM; the reason is that the weight function of the former adopted the basis function of the quadratic NURBS while the weight function of the latter used a linear Lagrange interpolation function. Concerning the 4-node NMM, the slope of the error curve for local refinement is greater than that for global refinement. In addition, after processing ME including the arc edge, NMM demonstrates higher accuracy.

7.2 Finite plate with a central edge crack under uniaxial tension

As shown in Figure 21, a finite rectangular plate with a central edge crack whose length is a, is subjected to uniform axial tension. The uniaxial tension (σ), the length (L) and width (W) of the plate are 4, 3, and 1 respectively. The theoretical solution for the problem is [29]

$$K_I = \sigma\sqrt{\pi a}F\left(\frac{a}{w}\right), \tag{41}$$

where

$$F(x) = 1.12 - 0.231x + 10.55x^2 - 21.72x^3 + 30.39x^4. \tag{42}$$

The stress intensity factors (SIFs), for different values of a, are calculated. Two different mathematical meshes, as shown in Figures 22(a) and (b) which show global and local refinements in the crack area respectively, are used to the

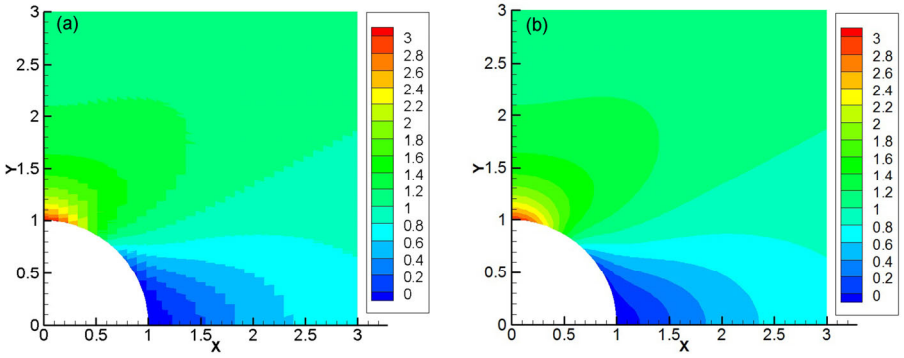

Figure 18 Distribution of σ_x in plate for two methods. (a) 4-node NMM; (b) 9-node NMM.

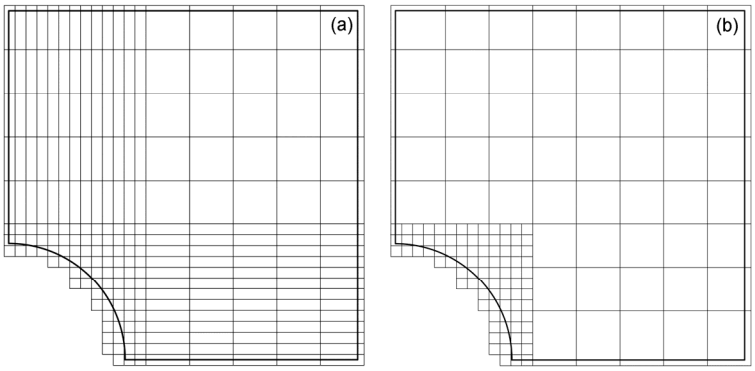

Figure 19 Mathematical mesh refinement for 'mode 1′. (a) Global refinement; (b) local refinement.

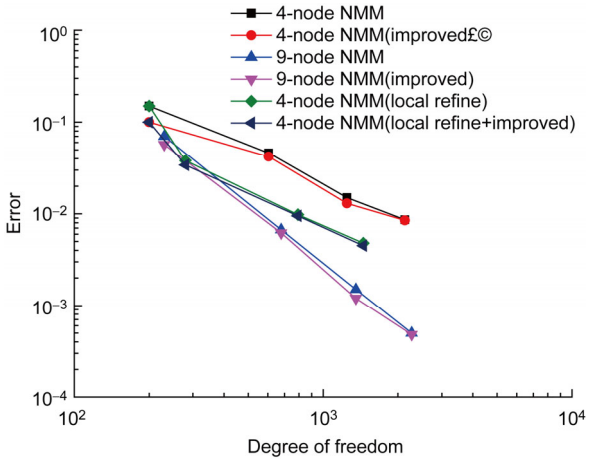

Figure 20 Error in stress (σ_x) at the top of the arc for different methods.

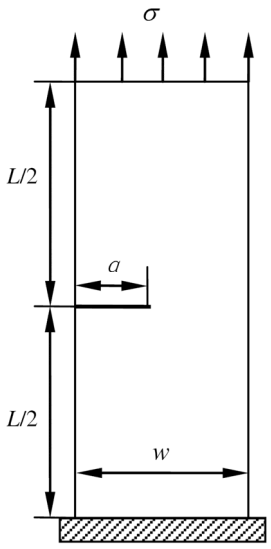

Figure 21 Finite plate with crack.

4-node NMM. The global refinement of the mathematical mesh shown in Figure 22(a) is also used to the 9-node NMM. SIFs calculated by the 4-node and 9-node NMMs based on different crack length models are listed in Tables 1 and 2. In terms of 4-node NMM, mesh 2 shows more advantages than mesh 1. Namely, under the same calculation accuracy, the number of degrees of freedom of mesh 2 is much less than that of mesh 1. Besides, under the conditions of the same MC mesh, the calculation accuracy of the 9-node NMM is higher than that of the 4-node NMM.

7.3 Disc with a central crack under concentrated load

As shown in Figure 23, for a disc with radius R and a central crack of length $2a$, two concentrated forces P are ap-

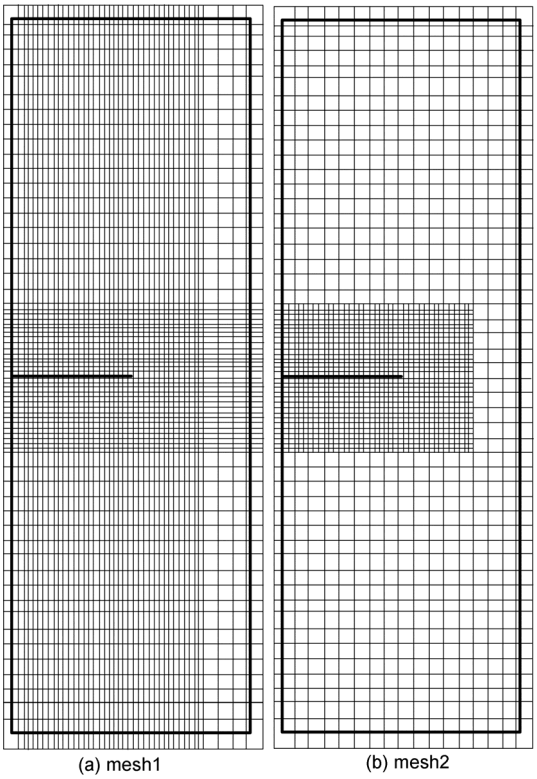

Figure 22 Mathematical mesh refinement for 'mode 2'. (a) Global refinement; (b) local refinement.

Table 1 SIFs results for 4-node NMM

a/*w*	Exact solution K_I	4-node NMM					
		Mesh1			Mesh2		
		DOFs	K_I	Error (%)	DOFs	K_I	Error (%)
0.1	0.8392	5126	0.8432	0.48	3926	0.8436	0.27
0.2	1.3743	5130	1.3707	0.26	3928	1.3711	0.23
0.3	2.0383	5134	2.0185	0.97	3930	2.0154	1.12
0.4	2.9827	5138	2.9652	0.58	3932	2.9640	0.63
0.5	4.4807	5142	4.4352	1.01	3934	4.4319	1.09
0.6	6.9925	5146	6.7887	2.91	3936	6.8121	2.58

Table 2 SIFs results for 9-node NMM

a/*w*	Exact solution K_I	9-node NMM		
		Mesh1		
		DOFs	K_I	Error (%)
0.1	0.8392	5108	0.8378	0.17
0.2	1.3743	5110	1.3764	0.15
0.3	2.0383	5112	2.0366	0.23
0.4	2.9827	5114	2.9740	0.29
0.5	4.4807	5116	4.4532	0.61
0.6	6.9925	5118	6.9663	0.37

plied across a diameter which overlaps the crack. The reference solution of SIFs for this problem is obtained from the Chinese Aeronautical Establishment [30]

$$K_I = F\left(\frac{a}{R}\right)\sigma\sqrt{\pi a}, \tag{43}$$

where

$$\sigma = P/(\pi R), \tag{44}$$

$$\begin{aligned} &F(x) \\ &= (1-0.4964x+1.5582x^2-3.1818x^3+10.0962x^4 \\ &\quad -20.7782x^5+20.1342x^6-7.5067x^7)/\sqrt{1-x}. \end{aligned} \tag{45}$$

Model parameters include R = 1, a = 0.3, P = 1, a Young's modulus E = 1000, and Poisson's ratio v = 0.3. The global and local mesh refinements, as shown in Figures 24(a) and (b), are used to the 4-node NMM. To the 9-node NMM, we also use global mesh refinements around the crack, shown in Figure 24(a), as the mathematical mesh. The arc edge problem is handled using two methods: approximate replacement of the arc edge, and exact integration over the manifold element containing the arc edge.

Based on the aforementioned models, the reference solution of K_I is 0.3507. Table 3 shows the calculated SIFs: this suggested that, with the same mathematical cover mesh, the 9-node NMM was more accurate than the 4-node NMM. Through exact integration of ME with arc edge, the accuracy of both the 9-node NMM and 4-node NMM improves. The global and local refinements of the MC mesh show significantly different numbers of degrees of freedom while the calculated SIFs are slightly different.

8 Conclusions and future prospects

This research proposes an NMM based on isogeometric analysis and derives the computation formula for the 9-node NMM using quadratic NURBS. In addition, for problems with arc edge, it proposes a numerical integration method of coordinate transformation based on the basis function of the NURBS curve. With regard to the 4-node NMM, a local refinement method of the mathematical mesh is proposed.

The results from three examples indicated that, compared with the 4-node NMM, the 9-node NMM based on the

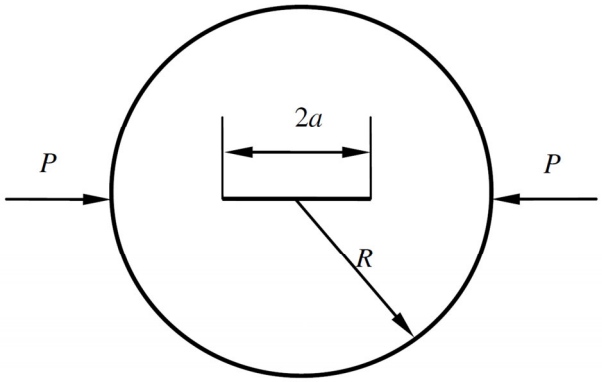

Figure 23 Circular plate with central crack.

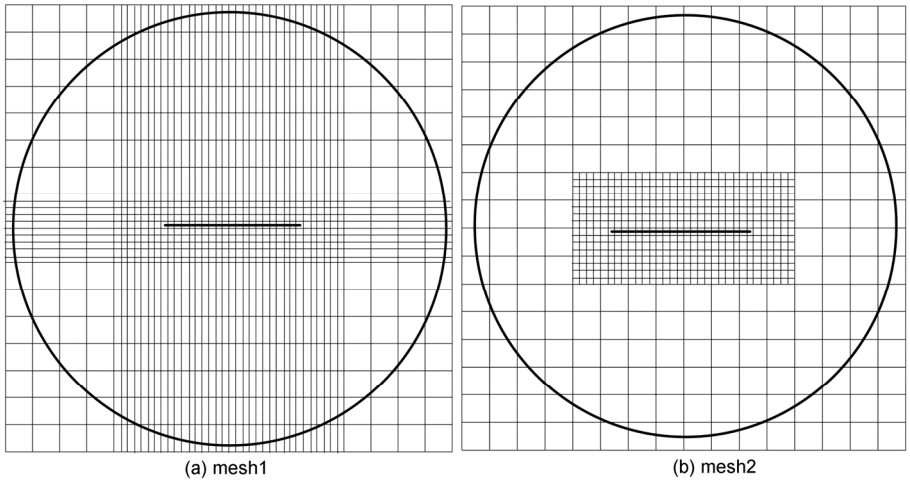

Figure 24 Mathematical mesh refinement for 'mode 3′. (a) Global refinement; (b) local refinement.

Table 3 SIFs results for different methods

Method	4-node NMM		4-node NMM (improved)		9-node NMM	9-node NMM (improved)
Mesh	Mesh1	Mesh2	Mesh1	Mesh2	Mesh1	Mesh1
DOFs	1928	1168	1928	1168	2152	2152
K_1	0.3451	0.3450	0.3456	0.3457	0.3476	0.3481
Error(%)	1.60	1.63	1.45	1.43	0.88	0.74

quadratic NURBS shows higher accuracies when solving both continuous and discontinuous problems. Besides, concerning the arc-contained boundary problem, the numerical integration method of coordinate transformation according to the basis function of the NURBS curve presents higher accuracies. In addition, while maintaining calculation accuracy, local mesh refinement using the 4-node NMM reduces the number of degrees of freedom.

Similar to the 9-node NMM, the 16-node NMM can be defined by changing the structural form of the mathematical cover so as to improve the order of the displacement function. For problems containing hyperbolae, ellipses, etc., methods for expressing the corresponding NURBS curves can be explored to define the corresponding coordinate transformation and therefore achieve exact integration for such problems.

This work was supported by the National Basic Research Program of China ("973" Project) (Grant No. 2014CB047100), and the National Natural Science Foundation of China (Grant No. 41372316).

1 Shi G H. Manifold method of material analysis. In: Transaction of the 9th Army Conference on Applied Mathematics and Computing, Report No. 92-1, U.S. Army Research office, Minneapolis, MN,1991. 57–76
2 Shi G H, Pei J M. Numerical Manifold Method and Discontinue Deformation Analysis (in Chinese). Beijing: Tsinghua University Press, 1997. 29–56
3 Zheng H, Xu D D. New strategies for some issues of numerical manifold method in simulation of crack propagation. Int J Numer Meth Eng, 2014, 97: 986–1010
4 Ma G W, An X M, He L. The numerical manifold method: A review. Int J Comp Meth-Sing, 2010, 7: 1–32
5 Wu Z J, Wong L N Y. Friction crack initiation and propagation analysis using the numerical manifold method. Comput Geotech, 2012, 39: 38–53
6 Wu Z J, Wong L N Y. Underground rockfall stability analysis using the numerical manifold method. Adv Eng Software, 2014, 76: 69–85
7 Jiang Q H, Deng S S, Zhou C B. Study of three-dimensional high-order numerical manifold method (in Chinese). Rock Soil Mechanics, 2006, 27: 1471–1474
8 Zhang G X, Sugiura Y, Hiroo H, et al. The second order manifold method with six node triangle mesh. J Struct Mech Earthquake Eng JSCE, 2002, 696: l–9
9 Chen G Q, Ohnishi Y, Ito T. Development of high-order manifold method. Int J Numer Meth Eng, 1998, 43: 685–712
10 Tesay R J, Chiou Y J, Chuang W L. Crack growth prediction by manifold method. J Eng Mech-ASCE, 1999, 125: 884–90
11 Chiou Y J, Lee Y M, Tesay R J. Mix mode fracture propagation by manifold method. Int J Fract, 2002, 114: 327–347
12 Yang S K, Ma G W, Ren X H, et al. Cover refinement of numerical manifold for crack propagation simulation. Eng Anal Bound Elem, 2014, 43: 37–49
13 Hughes T J R, Cottrell J A, Bazilevs Y. Isogeometric analysis: CAD, finite elements, NURBS, exact geometry and mesh refinement. Comput Method Appl M, 2005, 194: 4135–4195
14 Ge J L, Yang G L, Lu J. Advance in isogeometric analysis (in Chinese). Adv Mech, 2012, 42: 771–784.
15 Fischer P, Klassen M, Mergheim J, et al. Isogeometric analysis of 2D gradient elasticity. Comput Mech, 2011, 47: 325–334
16 Lin G, Zhang Y, Hu Z, et al. Scaled boundary isogeometric analysis for 2D elastostatics. Sci China-Phys Mech Astron, 2014, 2: 286–300
17 Piegl L, Tiller W. The NURBS Book. Berlin: Springer-Verlag Berlin and Heidelberg GmbH, 1997. 292–295
18 Sederberg T W, Zheng J, Bakenov A, et al. T-splines and T-nurccs. Acm T Graphic, 2003, 22: 477–484
19 Sederberg T W, Cardon D L, Finnigan G T, et al. T-splines simplification and local refinement. Acm T Graphic, 2003, 23: 276–283
20 Bazilevs Y, Calo V M, Cottrell J A, et al. Isogeometric analysis using T-splines. Comput Method Appl M, 2010, 199: 229–263
21 Zhang H H, Chen Y L, Li L X, et al. Accuracy comparison of rectangular and triangular mathematical elements in the numerical man-

ifold method. ICADD9, 2010. 297–303
22 Ma G W, An X M, Zhang H H, et al, Modelling complex crack problems using the numerical manifold method. Int J Fract, 2009, 156: 21–35
23 Moes N, Dolbow J, Belytschko I. A finite element method for crack growth without remeshing. Int J Nurner Methods Eng, 1999, 46: 131–150
24 Zhang H H, Li L X, An X M, et al. Numerical analysis of 2-D crack propagation problems using the numerical manifold method. Eng Anal Bound Elem, 2010, 34: 41–50
Cox M G. The numerical evaluation of B-Splines. J Inst Math Appl, 1972, 10: 134–149
25 Carl D B. On calculating with B-Splines. J Approx Theory, 1972, 6: 50–62
26 Wang X C. Finite Element Method. Beijing: Tsinghua University Press, 2003. 131–136
27 Timoshenko S P, Goodier J N. Theory of Elasticity. 3rd ed. New York: McGraw-Hill, 1970. 78–81
28 Zhang X M, Wan L, Yan B, et al. Fracture Mechanics. Beijing: Tsinghua University Press, 2012. 144–145
29 Chinese Aeronautical Establishment. Handbook of the Stress Intensity Factor (in Chinese). Beijing: Science Press, 1993. 145–167